



High-performance terahertz refractive index sensor based on a hybrid graphene Tamm structure

JINLEI Hu,¹ MENGHAN Li,¹ ZEXIANG WANG,¹ ZHENGDA Hu,¹ JICHENG WANG,^{1,2,*} ID SERGEI KHAKHOMOV,³ ID AND IGOR SEMCHENKO³

¹School of Science, Jiangsu Provincial Research Center of Light Industrial Optoelectronic Engineering and Technology, Jiangnan University, Wuxi 214122, China

²State Key Laboratory of Applied Optics, Changchun Institute of Optics, Fine Mechanics and Physics, Chinese Academy of Sciences, Changchun 130033, China

³Department of Optics, Francisk Skorina Gomel State University, Gomel 246019, Belarus

*Corresponding author: jcwang@jiangnan.edu.cn

Received 19 May 2021; revised 7 July 2021; accepted 15 July 2021; posted 19 July 2021 (Doc. ID 431912); published 11 August 2021

In recent years, the research on tunable and high-performance terahertz devices has attracted widespread attention. In this paper, we propose a novel refractive index sensor consisting of monolayer graphene and multilayer photonic crystal with a defect layer. It is found that Tamm plasmon polaritons can be excited at the top graphene interface, which can strongly interact with the defect mode in this coupled structure. The results of numerical simulation demonstrate that the coupling can be either tuned by adjusting the geometric parameters or actively controlled by the chemical potential in graphene as well as the incident angle of light, allowing for tunable dual-band perfect absorption with strong interaction. Moreover, the resonance frequency of the defect mode is sensitive to the changes of the ambient refractive index. The sensitivity and figure of merit of this device as a sensor can reach 1.01 THz per refractive index unit (THz/RIU) and 631.2 RIU⁻¹, respectively. In addition to high performance, the sensor does not require phase- or polarization-matching devices, paving the way for the research of optical devices. © 2021 Optical Society of America

<https://doi.org/10.1364/JOSAB.431912>

1. INTRODUCTION

Tamm plasmon polariton (TPP) mode is an optical surface mode that is strongly localized near the interface between a metal film and a multilayer photonic crystal (PC) [1,2]. The PC is a type of photonics device formed by periodically alternating arrangement of two dielectric films with different dielectric constants, and therefore the refractive index varies periodically in the arrangement direction [3–5]. When the spatial distribution period is about equal to the light wave, the electromagnetic wave transmission properties have a band structure similar to the semiconductor electron band, which is called the photonic energy band (PEG) [2–4]. The resonance generated by the TPP mode is attenuated from the interface to both sides due to the complex dielectric constants and photonic band gap (PBG) [6–9]. Graphene, as an emerging two-dimensional material, can replace the metal to excite the TPP mode under certain conditions because of its remarkable electrical, mechanical, and optical properties. The graphene-based TPP can be applied to the terahertz (THz) band with highly tunable performance and achieve more applications [10]. In contrast to the traditional surface-plasmon-polariton (SPP) mode, the TPP mode can

be excited at any incident angle in transverse-electric (TE) as well as transverse-magnetic (TM) polarization without using diffraction gratings or prisms [9–11]. Due to its strong local and slow-light properties, TPP mode has been successfully used in different applications such as narrowband thermal emission [11], confined Tamm plasmon lasers [12], and biosensors [13].

The coupling of TPP mode with other resonant modes can achieve extraordinary hybridization of the resonance polaritons [14–16], which can be used to tune the resonance frequency and guide the design of the nanostructures. For instance, TPP mode has been exploited to couple with defect states [14] for induced transparency, with magnetic plasmons [15] for large field enhancement, and with topological state for low-threshold and tunable optical bistability [16]. Among them, the defect mode is generated in the periodically destroyed multilayer PC, which is similar to the cavity mode when the original periodic multilayer structure is destroyed [17]. This mode demonstrates that a defect state with a very narrow frequency range appears in the structure, and the incident light whose frequency drops in this range will be captured by this PC microcavity [17,18].

The complex molecules have special spectral characteristics in the THz frequency range, where the radiation has low photonic energy and is non-ionizing [19]. Therefore, THz waves have been widely used in biological and chemical sensing [20,21]. Common THz time-domain spectroscopy methods have limitations in direct measurement of molecular resonance [22]. Another method is to use a structure with spectral properties, such as resonance, to study its sensitivity to the refractive index of an elastomer, and it does not interfere with the natural function of biomolecules [23].

In this paper, we have presented a novel THz refractive index sensor based on a graphene/PC/defect layer/PC hybrid Tamm system. The numerical studies show that the absorption resonance caused by the TPP has an asymmetric Fano resonance shape strongly coupling to the defect mode, which can be explained by coupled mode theory (CMT). The spectral properties of this structure can be passively tuned by the number of PC layers and actively tuned by the chemical potential of graphene and the incident angle of light. The resonance frequency of the absorption valley between the dual-band perfect absorption peaks is sensitive to the changes of the refractive index of the ambient layer. The results illustrate that the sensitivity and figure of merit (FoM) could reach 1.01 THz per refractive index unit (THz/RIU) and 631.2 RIU^{-1} , respectively, when the thickness of the ambient layer is 1300 μm and the incident angle is 10° . Due to its high performance, the proposed sensor may be considered a feasible alternative to previous high-performance complex structures.

2. STRUCTURE AND THEORY

As shown in Fig. 1(a), the multilayer PC is arranged alternately by poly 4-methyl-pentene (TPX) [24] and SiO_2 . The thickness of SiO_2 and TPX is set to $d_a = c/(4f_M \times n_a)$ and $d_b = c/(4f_M \times n_b)$, and the period length of the PC is $\Lambda = d_a + d_b$. f_M is the central frequency of the PC, and $n_a = 1.9$ and $n_b = 1.46$ are the refractive indices of SiO_2 and TPX, respectively. In Fig. 1(b), we show the band structure of the multilayer PC from the first to the fifth gaps with normal incident wave, i.e., $ky = 0$, when $f_M = 0.95 \text{ THz}$, $d_a = 41.52 \mu\text{m}$, and $d_b = 54.04 \mu\text{m}$. The widths of second and fourth PBGs are very narrow and even equal to no bandgap. The stereogram of the multilayer PC is illustrated in Fig. 1(c) corresponding to the band structure diagram in the Fig. 1(b). The reflectance spectrum of the multilayer PC structure is shown in Fig. 1(d). It basically verifies that the electromagnetic wave located in the PBG cannot propagate in the PC.

The graphene/PC structure that excites the graphene-based TPP mode is illustrated in Fig. 2(a). The resonance enhancement caused by the TPP mode [25] is generated and attenuated along the side of the PC with a period number $N = 11$. The other geometric parameters of the structure are the same as those used in Fig. 1. Graphene is modeled by an effective surface conductivity sheet, whose permittivity can be expressed as the formula $\epsilon_g = 1 + i\sigma_g/(\omega\epsilon_0 t)$ [26], where ω , ϵ_0 , and σ_g are the angular frequency, the permittivity of the vacuum, and the surface conductivity of graphene, respectively. The monolayer graphene is set to the surface current density in a COMSOL simulation because they are too thin.

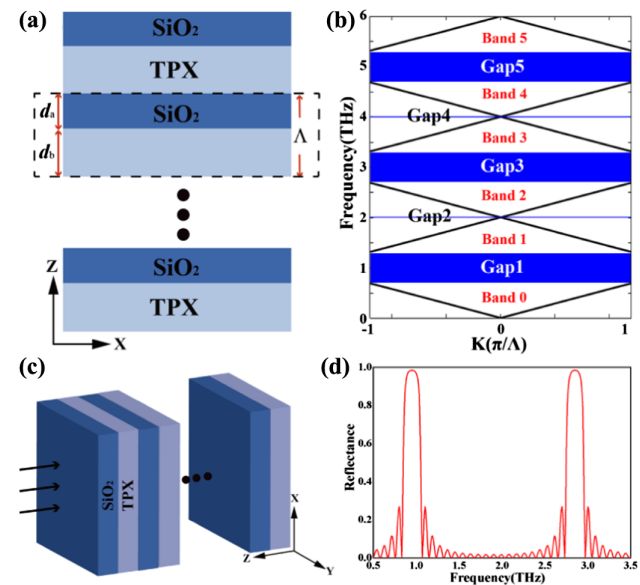


Fig. 1. (a) Multilayer PC periodically arranged with TPX and SiO_2 . (b) Band structure of the PC. (c) Three-dimensional structure diagram of the PC. (d) Reflectance spectrum of the multilayer PC structure.

In the THz regime, the surface conductivity σ_g of graphene can be defined by the Drude-like expression [27,28]

$$\sigma_g \approx \sigma_{\text{intra}} \approx \frac{e^2 \mu_c}{\pi \hbar^2} \frac{i}{\omega + i\tau^{-1}}, \quad (1)$$

where μ_c is the chemical potential, e is the electron charge, \hbar is the reduced Planck constant, and $\tau = \mu \mu_c / e v_F^2$ is the relaxation time. The chemical potential, Fermi velocity, and carrier mobility herein are chosen as $\mu_c = 0.66 \text{ eV}$, $v_F = 10^6 \text{ m/s}$, and $\mu = 1 \times 10^4 \text{ cm}^2/(\text{V} \cdot \text{s})$, respectively.

Spectra of absorption at normal incidence of the monolayer graphene/PC structure structure are shown in Fig. 2(b), which exhibits an asymmetric Fano line shape with a broader linewidth. The asymmetry of the absorption spectra can be attributed to the interference effect by the band edge mode of the PC. The position of the TPP resonance is $\omega_{\text{TPP}} = 0.954 \text{ THz}$, and the absoriton spectra can be analytically fitted by the Fano resonance model [29] via

$$A = \alpha \frac{(F\gamma + f - f_0)}{(f - f_0)^2 + \gamma^2}, \quad (2)$$

where f_0 and γ denote the resonance frequency and the damping rate, respectively; F is the Fano parameter describing the degree of asymmetry; and α is a balance modulus. According to Eq. (2) and the simulation results, the theoretically fitted absorption spectra for the TPP mode are shown in Fig. 2(a), coinciding excellently with the simulations. The fitting parameters for the TPP mode are $f_0 = 0.958 \text{ THz}$, $\gamma = 0.025 \text{ THz}$, $F = -2.5$, and $\alpha = 0.185$.

The resonance distribution of the defect mode excited at normal incidence in the PC/defect layer/PC structure is shown in Fig. 2(c). The geometric parameters of the PC structure are the same as those used in Fig. 2(a). The position of the defect mode is $\omega_D = 0.954 \text{ THz}$. The visible electric field is mainly distributed around the defect layer. Figure 2(d) illustrates the

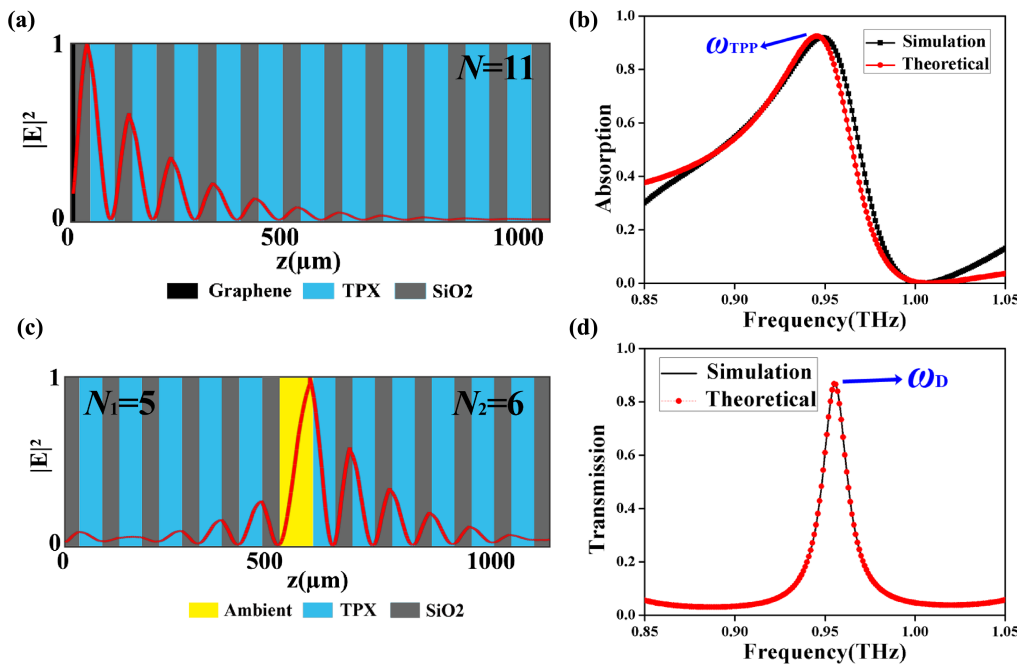


Fig. 2. (a) Schematic of monolayer graphene/multilayer PC structure and the TPP electric field intensity distribution line diagram. (b) The absorption spectra for the graphene/PC structure. (c) Schematic of multilayer PC with a defect layer and electric field distribution of the defect mode. (d) The transmission spectra for the multilayer PC with a defect layer.

transmission spectra for the PC/defect layer/PC structure, which shows that the defect mode can achieve a relatively narrow transmission peak. The spectra of the defect mode can be calculated by the transfer matrix method [30], whose results are given by the dots in Fig. 2(d), fitting well with the simulation results. The resonance wavelength of the defect mode can also be similarly expressed as the cavity mode resonance formula [10,31]

$$4\pi n_A \frac{d}{\lambda_D} + \Delta\phi = 2k\pi, \quad (3)$$

where integer k represents the order of the resonant mode. $\lambda_D = c/(n_A f_D)$ is the resonance wavelength and frequency, respectively. $\Delta\phi$ is the extra phase of the reflection at the cavity wall interface. Here $n_A = 1$ is the refractive index of the defect layer.

3. SIMULATIONS AND RESULTS

We construct a new hybrid Tamm structure composed of monolayer graphene and a multilayer PC with a defect layer as shown in Fig. 3(a). Coupling of two resonance modes can be theoretically described by the temporal CMT [32]. The absorption spectra for the graphene/PC/defect layer/PC hybrid system have been fitted by CMT in Fig. 3(b), which matches well with the simulated results. The material of the defect layer is the ambient, and its refractive index and thickness are $n_A = 1$ and $d = 75 \mu\text{m}$, respectively. The monolayer graphene is deposited on the top TPX with a thickness of $d_0 = 31.3 \mu\text{m}$. The multilayer PC is divided into upper and lower PCs by a defect layer, whose period numbers are $N_1 = 5$ and $N_2 = 11$, respectively. Our research is carried out under TM polarization, which means

that the incident wave only has an electric field distribution in the plane of incidence. In the simulation, we calculated the absorption spectra for this hybrid structure, which is shown in Fig. 3(b). There is a absorption valley at $\omega_D = 0.949 \text{ THz}$, and there are two peaks at $\omega_L = 0.932 \text{ THz}$ and $\omega_H = 0.972 \text{ THz}$. Here we denote the modes related to ω_L , ω_H , and ω_D as a lower-frequency mode (LFM), a higher-frequency mode (HFM), and a defect mode. This spectral response can be regarded as a typical electromagnetically induced transparency (EIT)-like profile. The physical mechanism can be understood as similar to the EIT in atomic systems [33]. For a typical three-level system, the ground state is represented by $|0\rangle$, and the upper states are represented by $|1\rangle$ and $|2\rangle$ (i.e., dark state) as shown in the inset of Fig. 3(b). The light is incident on graphene and excites the TPP mode, which can be analogue to the transition from $|0\rangle$ to $|1\rangle$ under the conditions of a “probe laser.” The narrow defect mode in a multilayer PC will be excited and coupled with the TPP mode, which can be similar to the transition between $|1\rangle$ and $|2\rangle$ without “pump light.” The coupling strength κ corresponds to the Rabi frequency [34]. Therefore, the two possible transition processes, namely, $|0\rangle \rightarrow |1\rangle$ and $|0\rangle \rightarrow |1\rangle \rightarrow |2\rangle \rightarrow |1\rangle$, will generate destructive interference owing to a π -phase difference. The destructive interference promotes the disappearing magnetic field of the TPP and produces narrow absorption valley in a wide absorption peak as shown in Fig. 3(b). The dissipation rates of the TPP and defect modes are denoted by γ_1 and γ_2 , respectively.

To further gain the physical insights on the strong coupling of TPP and defect modes, electromagnetic (EM) field distributions at the absorption peaks and valley at ω_L , ω_D , and ω_H for this hybrid mode are provided in Fig. 4. We clearly see that E and H field distributions at ω_L [Figs. 4(a) and 4(d)]

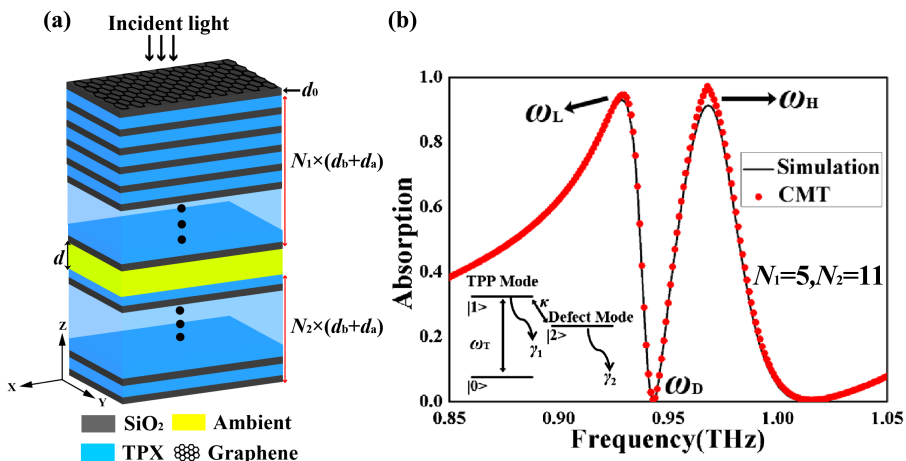


Fig. 3. (a) Proposed hybrid structure. (b) Absorption spectra for the monolayer graphene/PC/defect layer/PC hybrid structure, (i.e., $N_1 = 5$, $N_2 = 11$, $\mu_c = 0.66$ eV, $d_0 = 31.3$ μm , $d = 75$ μm , $d_a = 41.52$ μm , and $d_b = 54.04$ μm). The black curve and red dot stand for the COMSOL simulation and CMT results, respectively. The inset shows a three-level system.

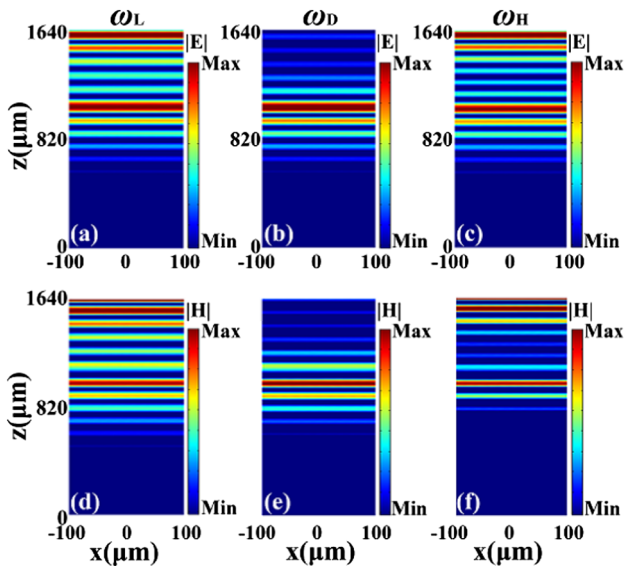


Fig. 4. (a)–(f) The normalized $|E|$ and $|H|$ field distributions at ω_L , ω_D , and ω_H , respectively. The left, middle, and right columns correspond to lower-frequency, defect, and higher-frequency modes, respectively.

and ω_H [Figs. 4(c) and 4(f)] exhibit the distinct hybridization features, namely, the enhanced EM fields are confined near the graphene/PC interface and around the defect layer, corresponding to the coupling of the TPP and defect modes. On the other hand, those at valley ω_D are mainly localized around the defect layer, displaying the typical characteristics of the defect mode [Figs. 4(b) and 4(e)], which essentially acts as a dark mode to destructively interfere with the TPP, forming a very deep transparent window.

Meanwhile, we explored the influence of different structural parameters such as the period number N_1 and N_2 of the asymmetric multilayer PC and the thickness d of the defect layer on the characteristics of the absorption spectra. Figure 5(a) depicts the absorption spectra of the hybrid structure for different N_1 . It shows that as the N_1 increases, the frequency interval

between the LFM and HFM becomes smaller, and the defect mode absorption valley becomes narrower. It can be seen from Fig. 5(b) that as the N_2 of the PC below increases, the overall absorption increases, and the absorption valley corresponding to the defect mode is also lower. Figure 5(c) reflects the influence of the thickness of the defect layer on the absorption spectrum. The absorption curve has an overall blueshift, which is a reference for later application to the refractive index sensor.

It is well known that the chemical potential of graphene can be actively changed by chemical or electrical doping [35,36], enabling a dynamically tunable optical response in a graphene sheet. In addition, the resonance frequency of the TPP and defect modes can also be adjusted by changing the angle of incidence [37]. Therefore, it can be expected to actively adjust the coupling of the TPP and defect modes in the hybrid Tamm structure. Here we study the spectral characteristics of the two modes after coupling by varying chemical potential in the monolayer graphene and incident angle of light as shown in Figs. 6 and 7. The geometric parameters of the model are kept the same as those used in Fig. 3 with TM-polarized normal illumination.

With the geometric parameters of the structure being fixed, the resonance frequency of the defect mode is maintained near 0.949 THz. Specifically, when $\mu_c = 0.66$ eV, the resonant frequencies of the TPP and defect mode nearly coincide with each other, thus achieving a striking frequency splitting shown in Fig. 6(b). Also, the high double-frequency absorption is generated in the hybrid system. The resonance peak of the TPP mode will gradually shift from the resonance peak of the defect mode to the low-frequency direction as the chemical potential of graphene drops from 0.86 to 0.26 eV. Due to the resonant frequency detuning of these two coupling modes increasing, the absorption spectra exhibit typical Fano-like features. We noticed that the resonant absorption of the coupling system with different chemical potential of graphene can be maintained at a high level ($>89.5\%$). In addition, by fixing $\mu_c = 0.66$ eV, Fig. 7 illustrates that the absorption spectra of the structure has a certain sensitivity to the incident angle θ . As the θ increases, the resonance frequency of the mixed mode blueshifts to a higher

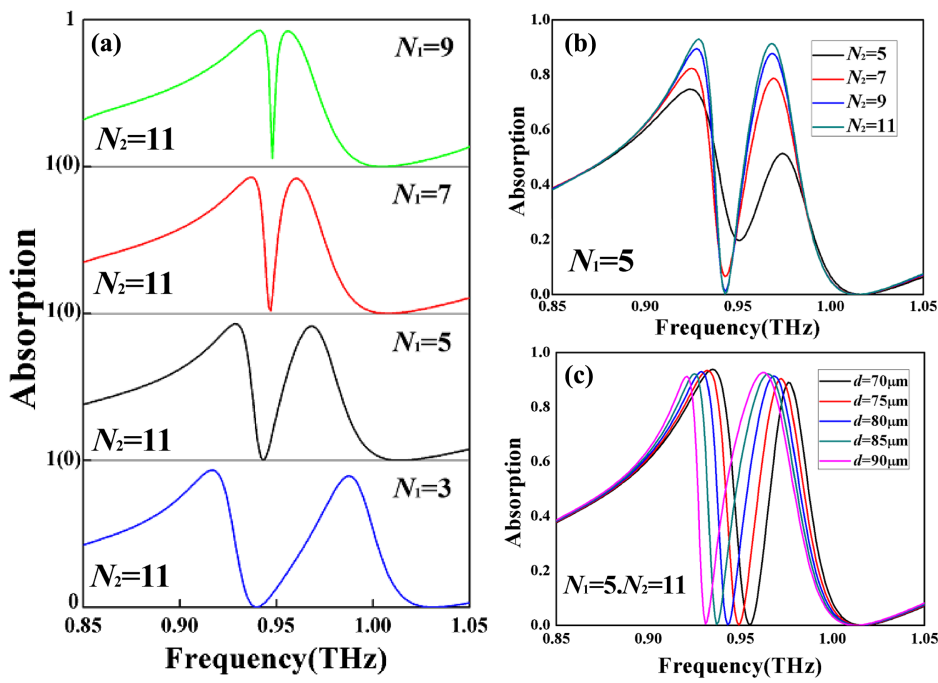


Fig. 5. Absorption spectra for the number of periods (a) N_1 and (b) N_2 of asymmetric multilayer PC, and (c) the thickness d of the defect layer. The geometric parameters of the structure are the same as those used in Fig. 3 with TM-polarized normal illumination.

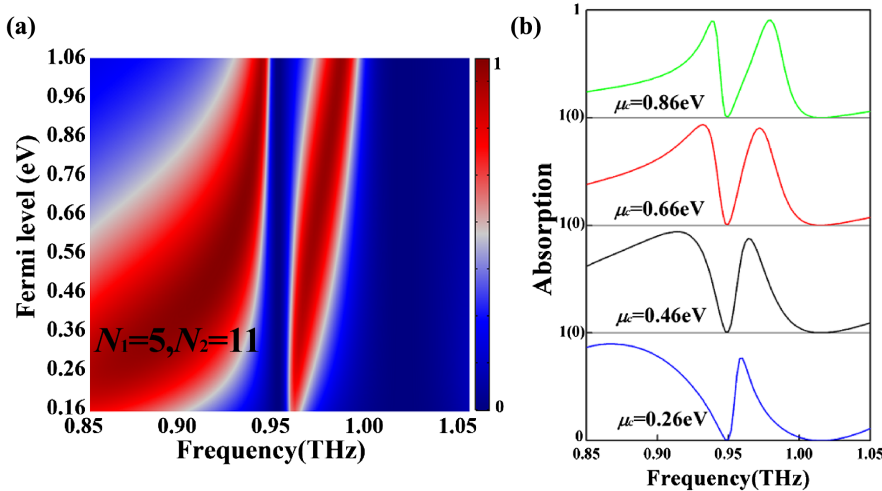


Fig. 6. (a) Evolution of absorption spectra of the hybrid structure for the graphene chemical potential. (b) The absorption curves for different chemical potential μ_c of 0.26, 0.46, 0.66, and 0.86 eV, where $N_1 = 5$ and $N_2 = 11$.

frequency. It is found that dual-band high absorption can be retained over the angle range from 0° to 18° .

Based on the relatively narrow absorption valley caused by the defect mode in the absorption spectra of the hybrid Tamm structure, we studied the performance of this refractive index sensor when the defect layer is used as the ambient layer. In order to obtain better performance, according to Fig. 5(a), we choose $N_1 = 9$ to achieve a relatively narrow absorption valley. Figure 8(a) shows the absorption spectra with different ambient refractive index n_A , where the thickness of the defect layer is $d = 1150 \mu\text{m}$ and $N_1 = 9$, and other structural parameters are the same as those in Fig. 3. According to the defect mode formula in Eq. (3), for a certain defect layer thickness d , there

are defect modes with different resonance frequencies in this THz frequency domain. When the resonant frequency of the defect mode is close to the resonant frequency of the TPP mode, the two modes will be coupled, and the refractive index sensor using the higher-order k defect mode has higher performance. Clearly, the resonance frequency of the defect mode depends on the refractive index of the ambient layer. Therefore, the ambient refractive index can be obtained by calculating the frequency of the absorption valley. As a result, the THz hybrid Tamm structure can indeed be used as a refractive index sensor.

Figure 8(b) shows the defect mode resonance frequencies for different refractive indices of the ambient layer. The resonant valley is redshifted to low frequencies from 0.967 to 0.961 THz

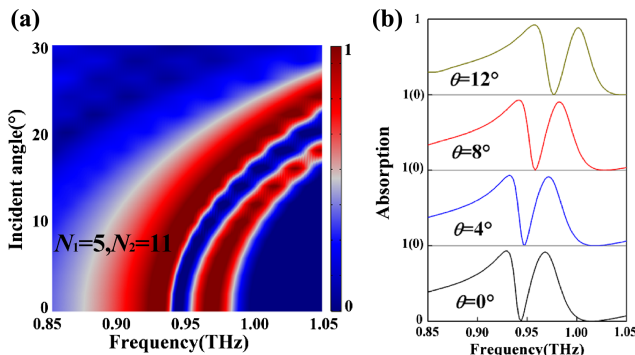


Fig. 7. (a) Evolution of absorption spectra of the hybrid structure for the incident angle. (b) The absorption curves for different incident angle $\theta = 0^{\circ}, 4^{\circ}, 8^{\circ}$, and 12° , where $N_1 = 5$ and $N_2 = 11$.

with the increase of the refractive index of the ambient layer from 1 to 1.01. The ratio between the change in the sensing sample refractive index Δn_A and the change in the resonant frequency Δf is called sensitivity (S) [38]; $S = \Delta f / \Delta n_A$, so the sensitivity at this time can reach 0.6 THz/RIU. The product of sensitivity and the reciprocal of full width at half-maximum (FWHM) of the resonant valley is called FoM [39]; $\text{FoM} = S / \text{FWHM}$. So the FoM of this structure is 260 RIU $^{-1}$.

In Fig. 8(c), the effect of the ambient layer thickness on sensitivity and the FoM is studied. It is clear that the FoM is directly proportional to the increase in the sample layer thickness. And the sensitivity increases dramatically from 0.143 to 0.6 THz/RIU with the increase of the thickness from 0 to 1150 μm . But for thicknesses higher than 1300 μm , the sensitivity seems to remain constant after a slight increase.

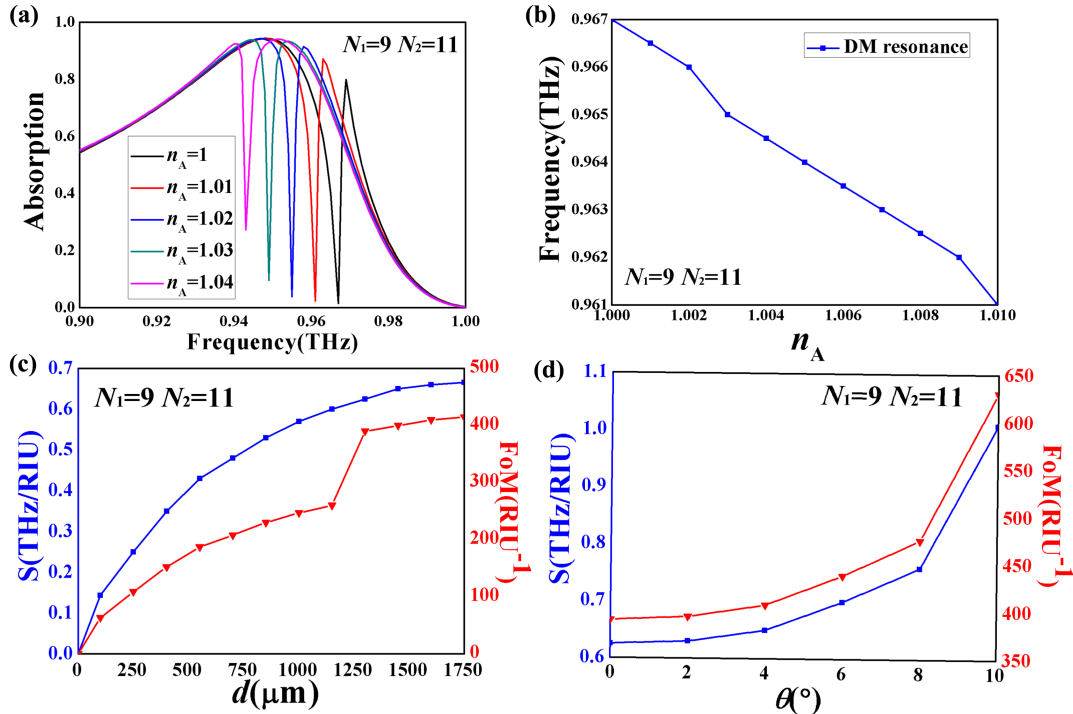


Fig. 8. (a) Absorption spectra and (b) defect resonance frequency of the sensor for various values of the ambient refractive index n_A with $d = 1150 \mu\text{m}$, $\mu_c = 0.66 \text{ eV}$, $N_1 = 9$, $N_2 = 11$, and $\theta = 0^{\circ}$; (c) effect of the ambient layer thickness d on S and the FoM; (d) effect of the incident angle θ on S and the FoM when $d = 1300 \mu\text{m}$.

Table 1. Comparison between the Proposed Sensor Performance and Other Sensors (NC = Not Counted)

| Reference (THz/RIU) | FoM (RIU $^{-1}$) | Q Factor | Materials |
|---------------------|--------------------|----------|------------------------------|
| [43], 2013 | 0.52 | 49 | 1124 Spoof plasmons |
| [41], 2017 | 6.65 | 1187 | NC SPR |
| [25], 2019 | 0.7 | 10.3 | NC Tamm with graphene |
| [44], 2020 | 0.9 | NC | 20 Dirac semimetal |
| [42], 2020 | 0.3 | 8.4 | 30 Metamaterial |
| [10], 2020 | 0.98 | 142 | NC TPP with cavity resonance |
| [45], 2020 | 0.5 | 12.4 | NC Dielectirc metasurface |
| This work | 1.01 | 631.2 | 593.7 TPP with defect mode |

At this time, the increasing trend of FoM becomes steeper due to the coupling of TPP with higher-order defect modes. As the incident angle increases, the sensitivity and FoM both increase significantly. In the range of $0^{\circ} \sim 10^{\circ}$, the sensitivity of the device reaches the best performance 1.01 THz/RIU when incident at an incident angle $\theta = 10^{\circ}$, where the FoM is increased to 631.2 RIU $^{-1}$. This increase is due to the increase of the optical path length through the structure with the increase of the incident angle.

In order to compare sensors operating at different frequencies, a normalized quality factor (Q factor) is also considered in Table 1. Q factor is defined as f_M / FWHM , where f_M is the center operating frequency of the sensor [40]. As observed in Table 1, compared with other THz sensors, the main advantage of our design is that its structure is simpler and easier to integrate with other system components.

For instance, plasmonic (SPR) structures such as [41] are implemented using the Otto configuration, requiring phase-matching prisms that make the structure bulky and delicate. They also need additional devices to adjust the polarization of the incident wave. All these factors make them difficult and costly in practice. Although the structure based on metamaterials has high performance, it also requires a complicated manufacturing process [42]. Our proposed sensor records a higher sensitivity and FoM with a simple and economical structure. The metal layer in the Tamm resonance structure can be replaced with graphene sheets and can record high performance. Due to the stability of the graphene and photonic crystal multi-layer structure, the proposed structure can solve the fabrication problems well.

4. CONCLUSIONS

In summary, we designed and studied a new type of graphene/PC/ambient layer/PC hybrid Tamm structure. The graphene-based TPP mode exhibits a typical Fano resonance line shape, which can couple with the defect mode excited in the PC/defect layer/PC structure. The strong coupling phenomenon is explained by CMT. The resonance frequency of the defect mode was sensitive to the change of the refractive index of the defect layer, so the performance of this hybrid structure as a sensor was studied. The simulation results showed that the sensitivity of the sensor could reach 1.01 THz/RIU when the thickness of ambient layer $d = 1300 \mu\text{m}$, and the FoM was 631.2 RIU^{-1} when incident angle was $\theta = 10^\circ$. The performance of the sensor could be improved by adjusting different structural parameters. As an emerging material, graphene has great advantages in terms of heat, electricity, and optics. The graphene-based TPP structure has high-efficiency tunable performance and could be applied to the THz frequency band to achieve more applications.

Funding. Undergraduate Research and Innovation Projects of Jiangnan University (2020366Y); Open Fund of State Key Laboratory of Applied Optics (SKLAO2020001A04); Intergovernmental Science and Technology Regular Meeting Exchange Project of Ministry of Science and Technology of China (CB02-20); National Natural Science Foundation of China (11811530052).

Disclosures. The authors declare no conflicts of interest.

Data Availability. The data that support the findings of this study are available from the corresponding author upon reasonable request.

REFERENCES

- Z. A. Zaky, A. M. Ahmed, A. S. Shalaby, and A. H. Aly, "Refractive index gas sensor based on the Tamm state in a one-dimensional photonic crystal: theoretical optimisation," *Sci. Rep.* **10**, 9736 (2020).
- Z. H. Lan, J. W. You, and N. C. Panoiu, "Nonlinear one-way edge-mode interactions for frequency mixing in topological photonic crystals," *Phys. Rev. B* **101**, 155422 (2020).
- M. Plihal and A. A. Maradudin, "Photonic band structure of two-dimensional systems: the triangular lattice," *Phys. Rev. B* **44**, 8565–8571 (1991).
- R. Zhao, G. D. Xie, M. Chen, Z. Lan, and W. Sha, "First-principle calculation of Chern number in gyrotropic photonic crystals," *Opt. Express* **28**, 4638–4649 (2020).
- A. H. Aly, A. M. Ahmed, and M. Shaban, "Multilayer angular optical filter as a smart window," *Indian J. Phys.* **94**, 95–103 (2019).
- X. Wang, J. Wang, D. Liu, Z. D. Hu, and F. Zhang, "Perfect absorption of molybdenum disulfide-based modified Tamm plasmonic structures," *Appl. Phys. Express* **11**, 062601 (2018).
- S. E. Abd El-Ghany, W. M. Noum, Z. Matar, Z. A. Zaky, and A. H. Aly, "Optimized bio-photonic sensor using 1D-photonic crystals as a blood hemoglobin sensor," *Phys. Scr.* **96**, 035501 (2020).
- H. Lu, Y. Li, Z. Yue, D. Mao, and J. Zhao, "Topological insulator based Tamm plasmon polaritons," *APL Photon.* **4**, 040801 (2019).
- W. Liang, Z. Xiao, H. Xu, H. Deng, and Y. Long, "Ultranarrow-bandwidth planar hot electron photodetector based on coupled dual Tamm plasmons," *Opt. Express* **28**, 31330–31344 (2020).
- M. M. Keshavarz and A. Alighanbari, "Self-referenced terahertz refractive index sensor based on cavity resonance and Tamm plasmonic modes," *Appl. Opt.* **59**, 4517–4526 (2020).
- Z. Wang, J. K. Clark, Y. L. Ho, B. Vilquin, H. Daiguji, and J. J. Delaunay, "Narrowband thermal emission from Tamm plasmons of a modified distributed Bragg reflector," *Appl. Phys. Lett.* **113**, 161104 (2018).
- C. Symonds, G. Lheureux, J. P. Hugonin, J. J. Greffet, and J. Bellessa, "Confined Tamm plasmon lasers," *Nano Lett.* **13**, 3179 (2013).
- Z. A. Zaky and A. H. Aly, "Theoretical study of a tunable low-temperature photonic crystal sensor using dielectric-superconductor nanocomposite layers," *J. Supercond. Novel Magn.* **33**, 2983–2990 (2020).
- G. C. Dyer, G. R. Aizin, S. J. Allen, A. D. Allen, D. Bethke, J. L. Reno, and E. A. Shaner, "Induced transparency by coupling of Tamm and defect states in tunable terahertz plasmonic crystals," *Nat. Photonics* **7**, 925–930 (2013).
- H. Liu, X. Sun, F. Yao, Y. Pei, F. Huang, H. Yuan, and Y. Jiang, "Optical magnetic field enhancement through coupling magnetic plasmons to Tamm plasmons," *Opt. Express* **20**, 19160–19167 (2012).
- Y. Peng, J. Xu, S. Wang, H. Dong, and L. Jiang, "Low-threshold and tunable optical bistability based on topological edge state in one-dimensional photonic crystal heterostructure with graphene," *IEEE Access* **8**, 196386 (2020).
- R. Ozaki, M. Ozaki, and K. Yoshino, "Defect mode in one-dimensional photonic crystal with in-plane switchable nematic liquid crystal defect layer," *Jpn. J. Appl. Phys.* **43**, L1477–L1479 (2004).
- H. Lu, X. M. Liu, Y. K. Gong, D. Mao, and L. Wang, "Optical bistability in metal-insulator-metal plasmonic Bragg waveguides with Kerr nonlinear defects," *Appl. Opt.* **50**, 1307–1311 (2011).
- B. Ferguson and X. C. Zhang, "Materials for terahertz science and technology," *Nat. Mater.* **1**, 26–33 (2002).
- E. Pickwell and V. P. Wallace, "Biomedical applications of terahertz technology," *J. Phys. D* **39**, R301 (2006).
- M. Zhang and J. T. W. Yeow, "Nanotechnology-based terahertz biological sensing: a review of its current state and things to come," *IEEE Nanotechnol. Mag.* **10**(3), 30 (2016).
- W. Withayachumnankul, J. F. O. Hara, W. Cao, I. Al-Naib, and W. Zhang, "Limitation in thin-film sensing with transmission-mode terahertz time-domain spectroscopy," *Opt. Express* **22**, 972–986 (2014).
- G. Gauglitz and G. Proll, "Strategies for label-free optical detection," *Adv. Biochem. Eng. Biotechnol.* **109**, 395–432 (2008).
- M. Naftaly and R. E. Miles, "Terahertz time-domain spectroscopy: a new tool for the study of glasses in the far infrared," *J. Non-Cryst. Solids* **351**, 3341–3346 (2005).
- M. M. Keshavarz and A. Alighanbari, "Terahertz refractive index sensor based on Tamm plasmon-polaritons with graphene," *Appl. Opt.* **58**, 3604–3612 (2019).
- A. Vakil and N. Engheta, "Supplementary: transformation optics using graphene," *Science* **332**, 1291–1294 (2011).
- F. H. L. Koppens, D. E. Chang, and F. J. García, "Graphene plasmonics: a platform for strong light-matter interactions," *Nano Lett.* **11**, 3370–3377 (2011).
- Z. Bao, J. Wang, Z. D. Hu, A. Balmakou, S. Khakhomov, Y. Tang, and C. Zhang, "Coordinated multi-band angle insensitive selection absorber based on graphene metamaterials," *Opt. Express* **27**, 31435–31445 (2019).
- A. E. Miroshnichenko, S. Flach, and Y. S. Kivshar, "Fano resonances in nanoscale," *Rev. Mod. Phys.* **82**, 2257–2298 (2009).

30. M. Kohmoto, B. Sutherland, and K. Iguchi, "Localization of optics: quasiperiodic media," *Phys. Rev. Lett.* **58**, 2436–2438 (1987).
31. Y. Yao, J. Cai, J. Sun, Z. Zhang, and Q. Hua, "Fabrication and characterization of a wide-bandgap and high-Q terahertz distributed-Bragg-reflector micro cavities," *Opt. Commun.* **426**, 84–88 (2018).
32. S. H. Fan, W. Suh, and J. D. Joannopoulos, "Temporal coupled-mode theory for the Fano resonance in optical resonators," *J. Opt. Soc. Am. A* **20**, 569–572 (2003).
33. N. Liu, L. Langguth, T. Weiss, J. Kästel, M. Fleischhauer, T. Pfau, and H. Giessen, "Plasmonic analogue of electromagnetically induced transparency at the Drude damping limit," *Nat. Mater.* **8**, 758–762 (2009).
34. B. Peng, Ş. K. Özdemir, W. Chen, F. Nori, and L. Yang, "What is—and what is not—electromagnetically-induced transparency in whispering-gallery-microcavities," *Nat. Commun.* **5**, 5082 (2014).
35. H. Liu, Y. Liu, and D. Zhu, "Chemical doping of grapheme," *J. Mater. Chem.* **21**, 3335–3345 (2011).
36. J. Wang, C. Song, H. Jing, Z. D. Hu, and Z. Feng, "Tunable Fano resonance based on grating-coupled and graphene-based Otto configuration," *Opt. Express* **25**, 23880–23892 (2017).
37. S. M. Kumar and D. Ritwick, "Tamm-plasmon polaritons in one-dimensional photonic quasi-crystals," *Opt. Lett.* **43**, 362–365 (2018).
38. N. Ayyanar, G. T. Raja, M. Sharma, and D. S. Kumar, "Photonic crystal fiber based refractive index sensor for early detection of cancer," *IEEE Sens. J.* **18**, 7093–7099 (2018).
39. A. H. Aly, D. Mohamed, M. Mohaseb, N. S. Abdel-Gawaad, and Y. Trabelsi, "Biophotonic sensor for the detection of creatinine concentration in blood serum based on 1D photonic crystal," *RSC Adv.* **10**, 31765–31772 (2020).
40. A. Panda and P. P. Devi, "Photonic crystal biosensor for refractive index based cancerous cell detection," *Opt. Fiber Technol.* **54**, 102123 (2020).
41. Y. Huang, S. Zhong, H. Yao, and D. Cui, "Tunable ultrasensitive terahertz sensing based on surface plasmon polariton of doped monolayer graphene," *Phys. Status Solidi A* **214**, 1600550 (2017).
42. T. Chen, D. Zhang, F. Huang, Z. Li, and F. Hu, "Design of a terahertz metamaterial sensor based on split ring resonator nested square ring resonator," *Mater. Res. Express* **7**, 095802 (2020).
43. B. Ng, J. Wu, S. M. Hanham, A. I. Fernández-Domínguez, N. Klein, Y. F. Liew, M. B. H. Breese, M. Hong, and S. A. Maier, "Spoof plasmon surfaces: a novel platform for THz sensing," *Adv. Opt. Mater.* **1**, 543–548 (2013).
44. S. Yan, S. Song, and H. Zhang, "Dynamically tunable Fano resonance with high Q factor based on asymmetric Dirac semimetal split-ring structure," *Mater. Res. Express* **7**, 025041 (2020).
45. Y. Wang, D. Zhu, Z. Cui, L. Yue, X. Zhang, L. Hou, K. Zhang, and H. Hu, "Properties and sensing performance of all-dielectric metasurface THz absorbers," *IEEE Trans. Terahertz Sci. Technol.* **10**, 599–605 (2020).